Journal of ELECTRONIC MATERIALS, Vol. 47, No. 3, 2018
https://doi.org/10.1007/s11664-017-6021-8

Structural and Magnetic Properties Evolution of Co-Nd Substituted M-type Hexagonal Strontium Ferrites Synthesized by Ball-Milling-Assisted Ceramic Process

WEN CHEN,[1] WENWEI WU,[1,2,3,4] CHONG ZHOU,[1] SHIFANG ZHOU,[1] MIAOYU LI,[1] and YU NING[1]

1.—School of Chemistry and Chemical Engineering, Guangxi University, Nanning 530004, People's Republic of China. 2.—Guangxi Colleges and Universities Key Laboratory of Applied Chemistry Technology and Resource Development, Nanning 530004, People's Republic of China. 3.—e-mail: gxuwuwenwei@aliyun.com. 4.—e-mail: wuwenwei@gxu.edu.cn

M-type hexagonal $Sr_{1-x}Co_xNd_xFe_{12-x}O_{19}$ (x = 0, 0.08, 0.16, and 0.24) has been synthesized by ball milling, followed by calcination in air. The calcined products have been characterized by x-ray powder diffraction (XRD), scanning electron microscopy (SEM), Fourier transform infrared spectra, and vibrating sample magnetometry. XRD and SEM analyses confirm the formation of M-type Sr hexaferrite with platelet-like morphology when $Sr_{1-x}Co_xNd_xFe_{12-x}O_{19}$ (x = 0, 0.08, 0.16, and 0.24) precursors are calcined at 950°C in air for 2.5 h. Lattice parameters "a" and "c" values of $Sr_{1-x}Co_xNd_xFe_{12-x}O_{19}$ reflect a very small variation after doping of Nd^{3+} and Co^{2+} ions. Average crystallite size of $Sr_{1-x}Co_xNd_xFe_{12-x}O_{19}$ sample, calcined at 1150°C, decreased obviously after doping of Co^{2+} and Nd^{3+} ions. This is because the bond energy of Nd^{3+}-O^{2-} is much larger than that of Sr^{2+}-O^{2-}. Magnetic characterization indicates that all the samples exhibit good magnetic properties. Substitution of Sr^{2+} and Fe^{3+} ions by Nd^{3+} and Co^{2+} ions can improve the specific saturation magnetizations and remanence of $Sr_{1-x}Co_xNd_xFe_{12-x}O_{19}$. $Sr_{0.84}Co_{0.16}Nd_{0.16}Fe_{11.84}O_{19}$, calcined at 1050°C, has the highest specific saturation magnetization value (74.75 ± 0.60 emu/g), remanence (45.15 ± 0.32 emu/g), and magnetic moment (14.34 ± 0.11 μ_B); $SrFe_{12}O_{19}$, calcined at 1150°C, has the highest coercivity value (4037.01 ± 42.39 Oe). These magnetic parameters make this material a promising candidate for applications such as high-density magnetic recording and microwave absorbing materials.

Key words: M-type hexagonal Co-Nd-substituted Sr ferrites, magnetic properties, mechanochemical processing, x-ray diffraction

INTRODUCTION

Hexagonal ferrites are an important class of ferromagnetic materials,[1,2] which have been used in many fields. For example, permanent magnets, high-density magnetic recording, microwave absorbing, medical equipment, and electronic devices,[3–6] which is attributed to hexagonal ferrite having a relatively high Curie temperature, excellent magnetic properties and oxidation resistance, and low cost. Hexaferrites can be divided into six types on the basis of their crystal structure and chemical formula, M-, W-, Y-, X-, Z-, and U-type hexaferrites with general formulae $MFe_{12}O_{19}$, $MMe_2Fe_{16}O_{27}$, $MMe_2Fe_{12}O_{22}$, $M_2Me_2Fe_{28}O_{46}$, $M_2Me_2Fe_{24}O_{41}$, and $M_4Me_2Fe_{36}O_{60}$ (M = Ba, Sr, and Pb; Me is any divalent element), respectively.[4,7] Within hexaferrites, the composition and structure of M-type hexaferrites are the simplest. Its molecular unit is made of one S (S block consists of two

(Received August 30, 2017; accepted December 9, 2017; published online December 27, 2017)

spinel units) and one R block (R block consists of three hexagonal units), with an overlap of hexagonally and cubically packed layers.[8] Hexagonal M-type $SrFe_{12}O_{19}$ is an important hard magnetic material, which has many advantages. For example, higher values for specific saturation magnetization, coercivity, magnetocrystalline anisotropy, performance to cost ratio, good chemical stability, and high Curie temperature compared to barium ferrite ($BaFe_{12}O_{19}$).[9] In order to obtain hexagonal strontium (Sr) ferrites with appropriate magnetic properties, some studies have been carried out. For example, Sr^{2+} ions were substituted by rare earth ions (such as La^{3+}, Pr^{3+}, Nd^{3+}, and Sm^{3+}, etc.)[10–13]; Fe^{3+} ions have been substituted by different cations (such as Al^{3+}, La^{3+}, Gd^{3+}, Er^{3+}, Co^{2+}, Mn^{2+}, Nd^{3+}, Cr^{3+}, and Bi^{3+}, etc.).[14–19] In addition, hexagonal Sr ferrites underwent combined substitution (such as Zr-Cd, La-Cu, La-Co, Nd-Co, Co-Ti-Ba, etc.).[20–25]

Many studies have shown that the magnetic properties of hexagonal Sr-based ferrites depend greatly on the composition, synthesis method, and calcination temperature. For example, Xia et al.[26] synthesized M-type hexagonal $SrFe_{12}O_{19}$ by the hydrothermal method, followed by sintering at 1100°C in air. The obtained samples consisted of the main M-type hexagonal $SrFe_{12}O_{19}$ phase in combination with a small amount of a foreign $SrFeO_{3-x}$ phase, and the samples exhibited two-phase magnetic behaviors. Wang et al.[12] synthesized Nd-substituted Sr hexaferrite ($Sr_{1-x}Nd_xFe_{12}O_{19}$) plate-like particles by the hydrothermal method, then calcined them between 1100°C and 1250°C for 2 h in air. The results show that the Nd-Sr ratio of 1:8 increases the coercivity without causing any significant deterioration of the saturation magnetization and/or the remanence. Peng et al.[22] synthesized $Sr_{1-x}La_xFe_{12-x}Co_xO_{19}$ (x = 0–0.5) ferrites by conventional ceramic technology at 890°C using $SrCO_3$, Co_2O_3, La_2O_3, and Fe_2O_3 as starting materials. It was found that the obtained $Sr_{1-x}La_xFe_{12-x}Co_xO_{19}$ (x = 0.2 and 0.3) ferrites can provide improved magnetic properties (Ms > 62 emu/g and Hc > 4022 Oe). Zhang et al.[24] synthesized Nd-Co-substituted M-type strontium hexaferrites by the sol–gel autocombustion method, followed by calcination at 1200°C for 3 h in air, using strontium nitrate, cobalt nitrate, neodymium nitrate, and iron nitrate as starting materials. Specific saturation magnetization (58 emu/g) and coercivity (3802.4 Oe) reached a maximum at x = 0.2. However, to the best of our knowledge, there is no report available for the structure, lattice strain, and magnetic properties evolution of $Sr_{1-x}Co_xNd_xFe_{12-x}O_{19}$ (x = 0, 0.08, 0.16, and 0.24) synthesized by the ball milling, followed by calcination in air using $SrC_2O_4{\cdot}H_2O$, $FeC_2O_4{\cdot}2H_2O$, $Nd_2(C_2O_4)_3{\cdot}10H_2O$, and $CoC_2O_4{\cdot}2H_2O$ as raw materials.

In this paper, the hexaferrite $Sr_{1-x}Co_xNd_xFe_{12-x}O_{19}$ (x = 0, 0.08, 0.16, and 0.24) magnetic powders were synthesized by the ball-milling-assisted ceramic process. The evolution of structure, lattice strain, and magnetic properties of the samples has been studied systematically.

EXPERIMENTAL

All samples of M-type hexagonal ferrites $Sr_{1-x}Co_xNd_xFe_{12-x}O_{19}$ (x = 0, 0.08, 0.16, and 0.24) were synthesized by the ball-milling-assisted ceramic process.[27] The starting materials used in this study were $SrC_2O_4{\cdot}H_2O$, $FeC_2O_4{\cdot}2H_2O$, $Nd_2(C_2O_4)_3{\cdot}10H_2O$, and $CoC_2O_4{\cdot}2H_2O$ of analytical grade. First, mixtures of the starting materials were milled in a stainless steel ball-milling tank of 100 ml for 30 min with an angular velocity of 350 rpm, and a ball-to-powder weight ratio of about 15:1; then, the mixed powder was dried at 80°C in air for 5 h. Finally, the mixed powder was calcined at 950°C, 1050°C, and 1150°C for 2.5 h, respectively, at a heating rate of 2°C min^{-1} in air to produce M-type hexagonal $Sr_{1-x}Co_xNd_xFe_{12-x}O_{19}$.

The structural characterization of the calcined hexagonal ferrite samples was carried out using a X′pert PRO x-ray diffractometer (XRD), using Cu Kα radiation (λ = 0.15406 nm) at room temperature in the range of 2θ = 5–75° in order to investigate phase purity. The micromorphology of the calcined samples was investigated using a S-3400 scanning electron microscope (SEM). The Fourier transform infrared spectra (FT-IR) spectra of the calcined samples were recorded on a Nexus 470 Fourier transform IR instrument. Magnetic measurements were carried out using a Lake Shore 7410 vibrating sample magnetometer at room temperature and under an applied magnetic field up to 20 kOe.

RESULTS AND DISCUSSION

XRD and SEM Analyses of the Calcined Products

Figure 1 represents XRD patterns of $Sr_{1-x}Co_xNd_xFe_{12-x}O_{19}$ (x = 0, 0.08, 0.16, and 0.24) hexagonal ferrite samples calcined at different temperature for 2.5 h. The XRD patterns were indexed to be a hexagonal magnetoplumbite (M-type) crystal structure having space group P63/mmc(194) (JCPDF no. 33-1340). The XRD analysis of the x = 0.0 sample, calcined at 1150°C, confirm the formation of a mono-phase of M-type hexagonal $SrFe_{12}O_{19}$, while $Sr_{1-x}Co_xNd_xFe_{12-x}O_{19}$ (x = 0.08, 0.16, and 0.24) samples consist of the main M-type hexagonal $SrFe_{12}O_{19}$ phase in combination with a small amount of the α-Fe_2O_3 phase. The substitutions of Nd^{3+} and Co^{2+} ions for Sr^{2+} and Fe^{3+} ions do not change the M-type hexagonal ferrite crystalline structure of $MFe_{12}O_{19}$ except that the diffraction peaks shift slightly to a lower degree with the increase of substitution content between x = 0 and x = 0.16, then to a higher degree at x = 0.24 (Fig. 1-e). XRD data of $Sr_{1-x}Co_xNd_xFe_{12-x}O_{19}$ were refined

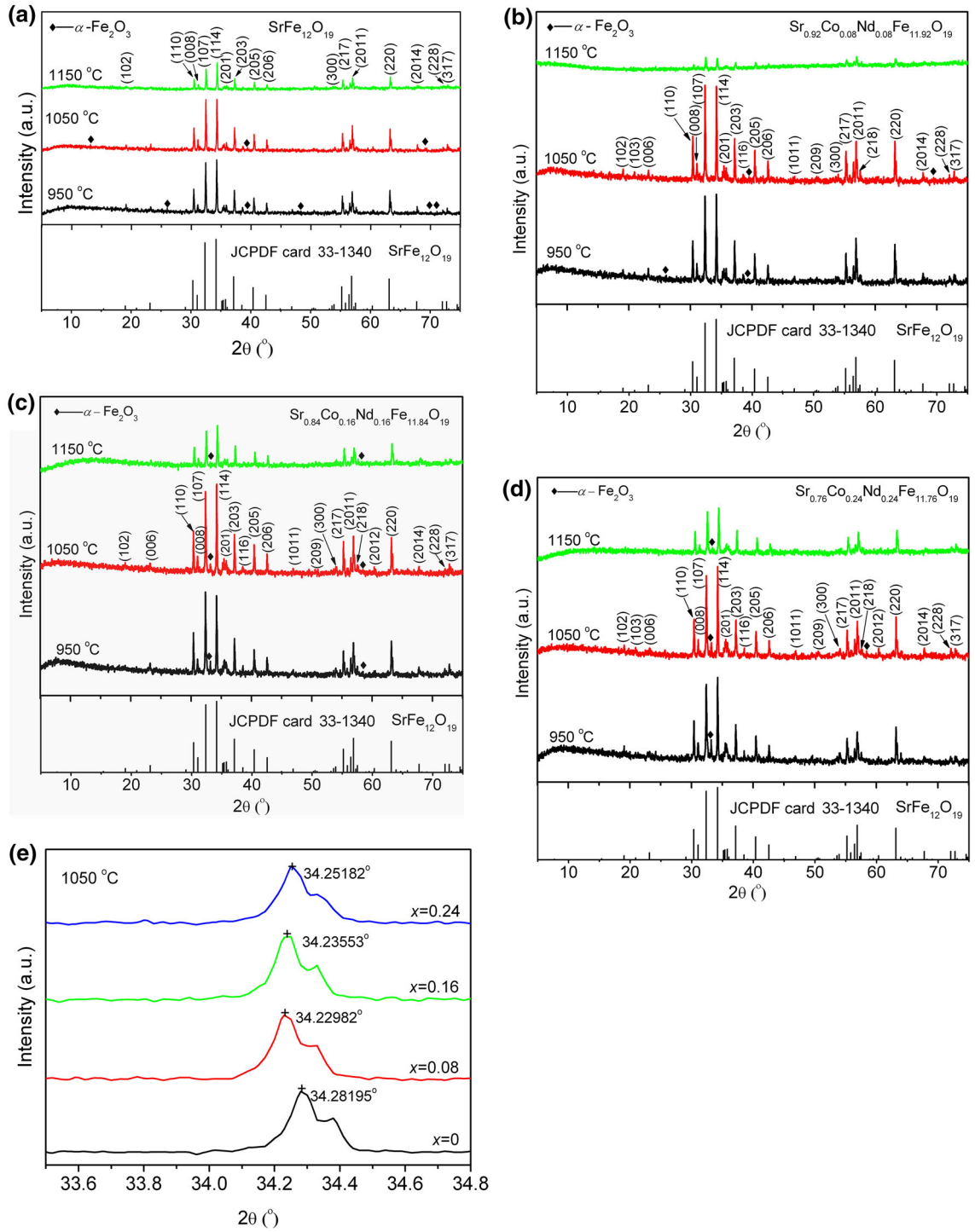

Fig. 1. XRD patterns of $Sr_{1-x}Co_xNd_xFe_{12-x}O_{19}$: (a) $SrFe_{12}O_{19}$, (b) $Sr_{0.92}Co_{0.08}Nd_{0.08}Fe_{11.92}O_{19}$, (c) $Sr_{0.84}Co_{0.16}Nd_{0.16}Fe_{11.84}O_{19}$, (d) $Sr_{0.76}Co_{0.24}Nd_{0.24}Fe_{11.76}O_{19}$, and (e) local magnification.

by the Rietveld method. The refined lattice parameter of $Sr_{1-x}Co_xNd_xFe_{12-x}O_{19}$, obtained at 1050°C, is listed in Table I. From Table I, the value of '*c*' value slightly increases with increasing substitution content (x), while '*a*' reflects a very small variation. This may be due to the smaller Nd^{3+} ion (0.099 nm)[8] substituting the larger Sr^{2+} ions (0.144 nm)[27]; the larger Co^{2+} ion (0.072 nm)[27] substitutes the smaller Fe^{3+} ions (0.067 nm).[8] Similar results are also reported for M-type hexagonal $BaNd_xFe_{12-x}O_{19}$ ferrites by Chen et al.[8] and M-type hexagonal $Sr_{1-x}La_xFe_{12-x}Cu_xO_{19}$ by Qiao et al.[24]

Table I. Structural properties of $Sr_{1-x}Co_xNd_xFe_{12-x}O_{19}$ calcined at 1050°C

Composition, x	a (nm)	c (nm)	c/a	Lattice strains (%)	d_{114} (nm)	Crystallite size (nm)
0.0	0.587 (5)	2.299 (2)	3.913 (6)	0.135 (8)	0.261 (4)	83.07 ± 1.33
0.08	0.587 (9)	2.302 (1)	3.915 (9)	0.126 (1)	0.261 (8)	92.44 ± 1.48
0.16	0.587 (9)	2.301 (7)	3.915 (2)	0.131 (7)	0.261 (7)	86.25 ± 1.38
0.24	0.587 (7)	2.300 (9)	3.915 (2)	0.130 (3)	0.261 (6)	79.09 ± 1.27

The crystallite size is calculated using the Scherrer formula[28] given by Eq. 1.

$$D = K\lambda/(\beta\cos\theta), \quad (1)$$

where D is the crystallite size, K the Scherrer constant equal to 0.89, λ the wave length (0.15406 nm), β the full width at half maxima, and θ the corresponding angle. In order to investigate the influence of the substitution of Co^{2+} and Nd^{3+} ions on the interplanar spacing of hexagonal $Sr_{1-x}Co_xNd_xFe_{12-x}O_{19}$, the $d_{(114)}$ interplanar spacing of $Sr_{1-x}Co_xNd_xFe_{12-x}O_{19}$ is calculated by the following Bragg equation.[28]

$$d_{(114)} = \frac{\lambda}{2\sin\theta_{(114)}}, \quad (2)$$

The crystallite size (D) of $Sr_{1-x}Co_xNd_xFe_{12-x}O_{19}$, obtained at different temperatures, and $d_{(114)}$ interplanar spacing of $Sr_{1-x}Co_xNd_xFe_{12-x}O_{19}$, calcined at 1050°C, are shown in Fig. 2 and Table I, respectively. From Fig. 2, the crystallite size of $Sr_{1-x}Co_xNd_xFe_{12-x}O_{19}$ at first increases with the increase in calcination temperature, and then decreases at 1150°C. In addition, the crystallite size of the $Sr_{1-x}Co_xNd_xFe_{12-x}O_{19}$ sample, calcined at 1150°C, decreases markedly after substituting Sr^{2+} and Fe^{3+} ions by Nd^{3+} and Co^{2+} ions. The trend of average crystallite size of $Sr_{1-x}Co_xNd_xFe_{12-x}O_{19}$, calcined at 1050°C, decreases with the increase in substitution content (x) (see Table I). The evolution of the average crystallite size of $Sr_{1-x}Co_xNd_xFe_{12-x}O_{19}$ with substitution content (x) can be explained as follows. The bond energy of Nd^{3+}–O^{2-} is much larger than that of Sr^{2+}–O^{2-}. When Nd^{3+} ion enters the hexagonal lattice to form the Nd^{3+}–O^{2-} bond, the crystal nucleation and growth of Nd^{3+}-Co^{2+} substituted $SrFe_{12}O_{19}$ will consume more energy, resulting in the decreases of average crystallite size with the increase in substitution content (x).[28] The $d_{(114)}$ values of the samples in Table I reveal that the interplanar spacing reflects a very small variation after doping Nd^{3+} and Co^{2+} ions.

The lattice strains (ε) of the $Sr_{1-x}Co_xNd_xFe_{12-x}O_{19}$ can be deduced using the following Williamson–Hall formula[28]:

$$\varepsilon = \frac{\beta}{4\tan\theta}, \quad (3)$$

where ε is the lattice strain of the structure, β the full width at half maximum (in radians) of the peaks, and θ the peak position. Lattice strains of $Sr_{1-x}Co_xNd_xFe_{12-x}O_{19}$, calcined at 1050°C, are shown in Table I. The trend of lattice strains decreases with the increase in substitution content (x). This is because the radius of Nd^{3+} ion (0.099 nm)[8] is smaller than that of the Sr^{2+} ion (0.144 nm),[27] and after the Sr^{2+} ions is substituted by Nd^{3+} ions with smaller ionic radii, the distortion of hexagonal structure in $Sr_{1-x}Co_xNd_xFe_{12-x}O_{19}$ decreases, resulting in the decrease of lattice strain in $Sr_{1-x}Co_xNd_xFe_{12-x}O_{19}$.

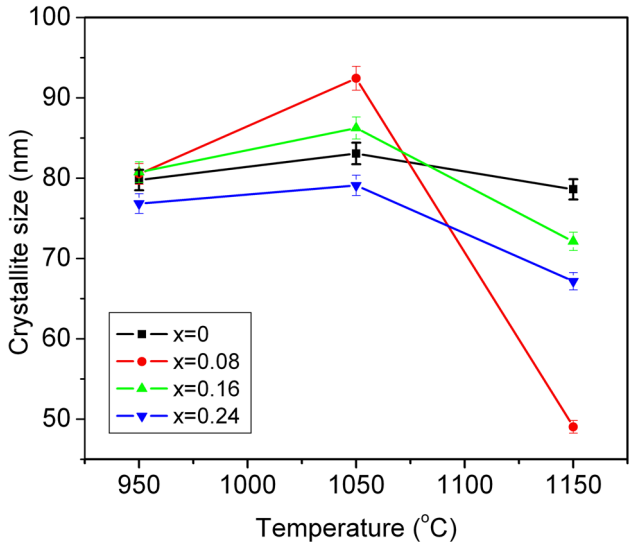

Fig. 2. Dependence of crystallite size of $Sr_{1-x}Co_xNd_xFe_{12-x}O_{19}$ on substitution content (x) and calcination temperature.

The crystallinity of $Sr_{1-x}Co_xNd_xFe_{12-x}O_{19}$ is estimated using Eq. 4 or Eq. 5[29,30]

$$\text{Crystallinity}(\%) = \frac{I_{\text{peaks of } SrFe_{12}O_{19}}}{I_{\text{all peaks}}}, \quad (4)$$

or

$$\text{Crystallinity}(\%) = \frac{A_{\text{peaks of } SrFe_{12}O_{19}}}{A_{\text{all peaks}}}, \quad (5)$$

where I is the intensity and A the area of the XRD peaks, respectively. The crystallinity of $Sr_{1-x}Co_xNd_xFe_{12-x}O_{19}$ (x = 0, 0.08, 0.16, and 0.24), obtained at different temperatures, is shown in Fig. 3. The crystallinity of $SrFe_{12}O_{19}$ and $Sr_{0.92}Co_{0.08}Nd_{0.08}Fe_{11.92}O_{19}$ first increases with the

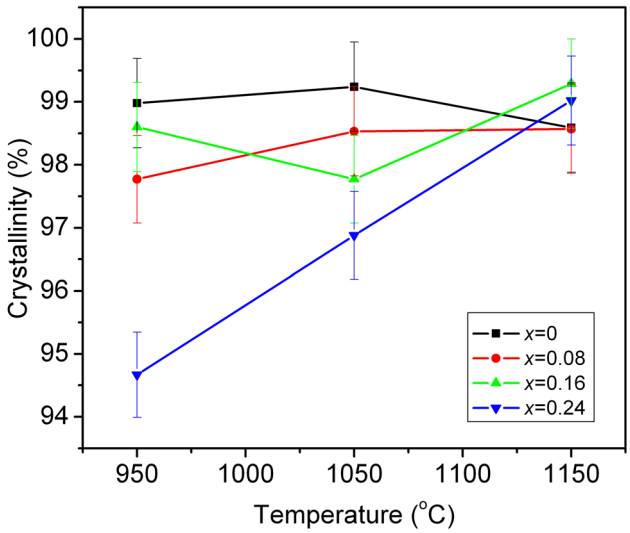

Fig. 3. Dependence of crystallinity of $Sr_{1-x}Co_xNd_xFe_{12-x}O_{19}$ on calcination temperature and substitution content (x).

increase in calcination temperature, and then decreases slightly at 1150°C. The crystallinity of $Sr_{0.84}Co_{0.16}Nd_{0.16}Fe_{11.84}O_{19}$ first decreases slightly with the increase in calcination temperature, and then increases at 1150°C. By contrast, the crystallinity of $Sr_{0.76}Co_{0.24}Nd_{0.24}Fe_{11.76}O_{19}$ increases linearly with the increase in calcination temperature. In addition, the crystallinity of $Sr_{1-x}Co_xNd_xFe_{12-x}O_{19}$, calcined at 1050°C, decreases with the increase in substitution content (x). However, after being calcined at 1150°C, the trend of the crystallinity of $Sr_{1-x}Co_xNd_xFe_{12-x}O_{19}$ increases with the increase in substitution content (x). This is because the radius of Nd^{3+} ion (0.099 nm)[8] is smaller than that of the Sr^{2+} ion (0.144 nm),[27] and the radius of Co^{2+} ion (0.072 nm)[27] is slightly larger than that of the Fe^{3+} ion (0.067 nm).[8] Nd^{3+} and Co^{2+} ions easily enter the lattice of hexagonal $SrFe_{12}O_{19}$ to a solid solution, which restrains the formation of the α-Fe_2O_4 phase.

Figure 4 shows the SEM micrographs of the M-type hexaferrite $Sr_{1-x}Co_xNd_xFe_{12-x}O_{19}$ (x = 0, 0.08, 0.16, and 0.24) calcined at 1050°C and 1150°C. It can be seen from the SEM micrographs that the grains show platelet-like shapes, as shown in Fig. 4a–h, and the particle size is obviously affected by calcination temperature. Particle size increases with the increase in calcination temperature. The particle size of $Sr_{1-x}Co_xNd_xFe_{12-x}O_{19}$, calcined at 1050°C, ranged from 300 nm to 1.5 μm. By contrast, the particle size of the sample, calcined at 1150°C, ranged from 700 nm to 3.0 μm. In addition, the trend of the particle size of $Sr_{1-x}Co_xNd_xFe_{12-x}O_{19}$ decreases with the increase in substitution content (x). Particle sizes determined by SEM were significantly larger than the values of average crystallite sizes from XRD technology, which can be attributed

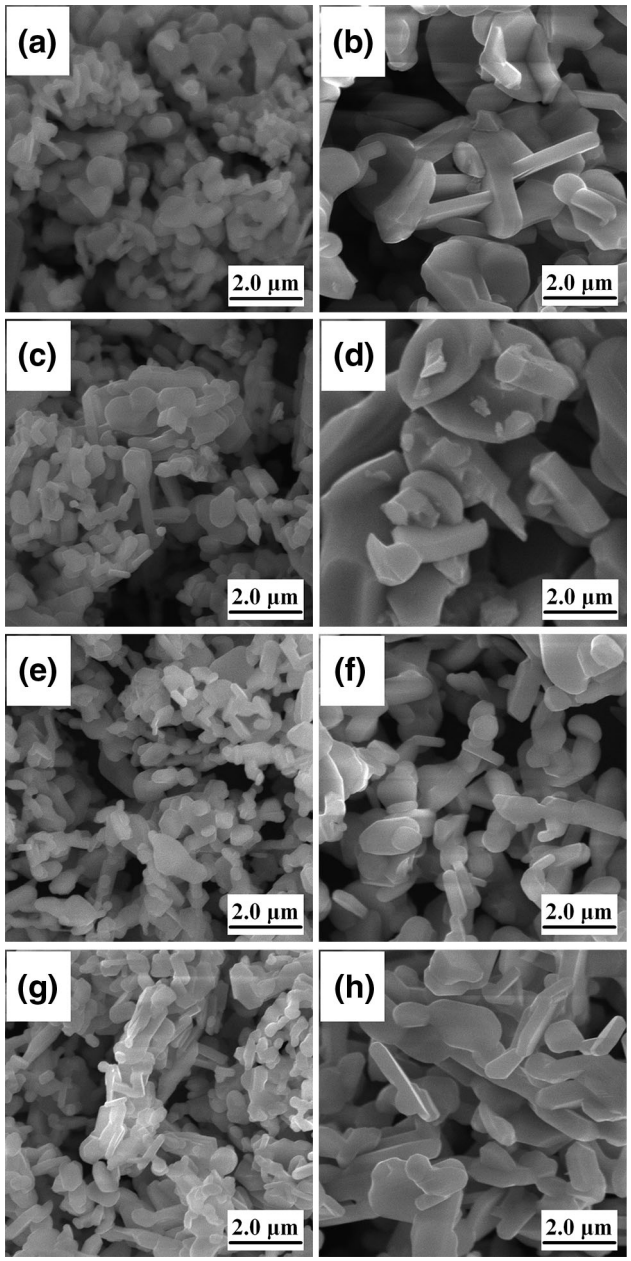

Fig. 4. SEM images of $Sr_{1-x}Co_xNd_xFe_{12-x}O_{19}$: $SrFe_{12}O_{19}$ (a-1050°C, b-1150°C), $Sr_{0.92}Co_{0.08}Nd_{0.08}Fe_{11.92}O_{19}$ (c-1050°C, d-1150°C), $Sr_{0.84}Co_{0.16}Nd_{0.16}Fe_{11.84}O_{19}$, (e-1050°C, f-1150°C), $Sr_{0.76}Co_{0.24}Nd_{0.24}Fe_{11.76}O_{19}$ (g-1050°C, h-1150°C).

to the fact that the values observed by SEM have the size of the secondary particles. In addition, the x-ray line broadening analysis disclosed only the size of a single crystallite.[31]

FT-IR Spectroscopic Analysis of $Sr_{1-x}Co_xNd_xFe_{12-x}O_{19}$

FT-IR spectra of $Sr_{1-x}Co_xNd_xFe_{12-x}O_{19}$ samples, calcined at 1050°C, are shown in Fig. 5. The positions of all the adsorption bands of the samples are

similar, while their relative intensities varied. The spectrum of $SrFe_{12}O_{19}$ sample shows three characteristic absorption bands in the region of 400–730 cm^{-1}, which is assigned to the Fe-O stretching vibration band in octahedral and tetrahedral sites of M-type hexagonal strontium ferrites.[32] Band at 447 cm^{-1} is assigned to Fe-O bending vibration by $Fe\text{-}O_4$ and Fe-O stretching mode by $Fe\text{-}O_6$. The band at 555 cm^{-1} is attributed to the Fe-O stretching vibration by $Fe\text{-}O_4$. The band at 598 cm^{-1} corresponds to the Sr-O stretching vibration band.[33,34] After substituting Sr^{2+} and Co^{2+} ions by Nd^{3+} and Co^{2+} ions, absorption bands of $Sr_{1-x}Co_xNd_xFe_{12-x}O_{19}$ (x = 0.08, 0.16, and 0.24) in the region of 400–730 cm^{-1} become weak (Fig. 5a). In addition, the bands at 447 cm^{-1} and 555 cm^{-1} shift to a lower wave number, and the band at 598 cm^{-1} shifts to a higher wave number (Fig. 5b). This is because the radius of Nd^{3+} ion (0.099 nm)[8] is smaller than that of the Sr^{2+} ion (0.144 nm),[27] and the radius of Co^{2+} ion (0.072 nm)[27] is slightly larger than that of the Fe^{3+} ion (0.067 nm).[8] In other words, the bond energy of $Nd^{3+}\text{-}O^{2-}$ bond is larger than that of $Sr^{2+}\text{-}O^{2-}$, and the bond energy of $Co^{2+}\text{-}O^{2-}$ bond is smaller than that of $Fe^{3+}\text{-}O^{2-}$.

Magnetic Properties of $Sr_{1-x}Co_xNd_xFe_{12-x}O_{19}$

Magnetic hysteresis loops of the hexaferrites $Sr_{1-x}Co_xNd_xFe_{12-x}O_{19}$ (x = 0, 0.08, 0.16, and 0.24) magnetic powders, calcined at different temperatures, are shown in Fig. 6. All samples with uniaxial anisotropy exhibit a broad M–H loop and rectangular shape, indicating that all $Sr_{1-x}Co_xNd_xFe_{12-x}O_{19}$ samples have a hard magnetic property. The dependence of specific saturation magnetization and lattice strains of $Sr_{1-x}Co_xNd_xFe_{12-x}O_{19}$ on substitution content (x) is shown in Fig. 7. As seen in Fig. 7a, the specific saturation magnetization of $Sr_{1-x}Co_xNd_xFe_{12-x}O_{19}$ (x = 0, 0.08, 0.16, and 0.24) first increases with the increase in calcination temperature, and then decreases at 1150°C. In addition, the specific saturation magnetization of $Sr_{1-x}Co_xNd_xFe_{12-x}O_{19}$ varies nonlinearly with the substitution content (x). The $Sr_{0.84}Co_{0.16}Nd_{0.16}Fe_{11.84}O_{19}$, obtained at 1050°C, has the highest specific saturation magnetization (74.75 ± 0.60 emu/g). Substitution of Sr^{2+} and Fe^{3+} ions by Nd^{3+} and Co^{2+} ions can improve the specific saturation magnetizations, which is attributed to the Nd^{3+} ion ($4f^3$, 3 μ_B) having a higher magnetic moment than the Sr^{2+} ion ($5\ s^0$, 0 μ_B). Similar results were also reported for M-type hexagonal $BaNd_xFe_{12-x}O_{19}$ ferrites by Chen et al.[8] The relationship between the specific saturation magnetization and lattice strains of $Sr_{1-x}Co_xNd_xFe_{12-x}O_{19}$ sample, calcined at 1050°C, is shown in Fig. 7b. Specific saturation magnetization increases with the increase in lattice strains. A similar phenomenon was also observed for strontium (Sr)-substituted cobalt ferrites ($Co_{1-x}Sr_xFe_2O_4$),[35]

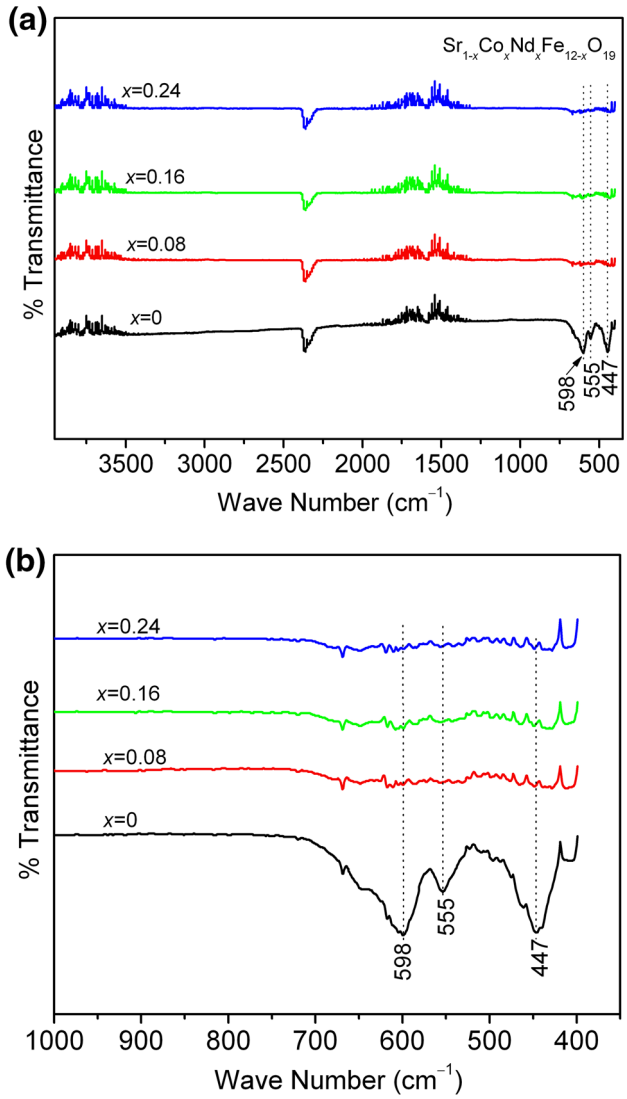

Fig. 5. FT-IR spectra of $Sr_{1-x}Co_xNd_xFe_{12-x}O_{19}$ calcined at 1050°C (a) and local magnification (b).

calcium (Ca)-substituted cobalt ferrite ($Co_{1-x}Ca_xFe_2O_4$),[36] and Sm-substituted Ba-Co hexaferrite ($BaCo_{0.8}Sm_xFe_{(11.2-x)}O_{19}$).[37]

The dependence of remanence (Mr) and coercivity (Hc) on calcination temperature and substitution content (x) is shown in Fig. 8. Remanence of $Sr_{1-x}Co_xNd_xFe_{12-x}O_{19}$ first increases with the increase in calcination temperature, and then decreases at 1150°C (Fig. 8a). In addition, the remanence trend of $Sr_{1-x}Co_xNd_xFe_{12-x}O_{19}$, calcined at 950°C and 1050°C, decreases with the increase in substitution content (x), except for $Sr_{0.84}Co_{0.16}Nd_{0.16}Fe_{11.84}O_{19}$. $Sr_{0.84}Co_{0.16}Nd_{0.16}Fe_{11.84}O_{19}$, calcined at 1050°C, has the highest remanence value (45.15 ± 0.32 emu/g); $SrFe_{12}O_{19}$, calcined at 1150°C, has the lowest remanence value (29.34 ± 0.21 emu/g). Coercivity of $Sr_{0.84}Co_{0.16}Nd_{0.16}Fe_{11.84}O_{19}$ decreases linearly with the increase in calcination temperature.

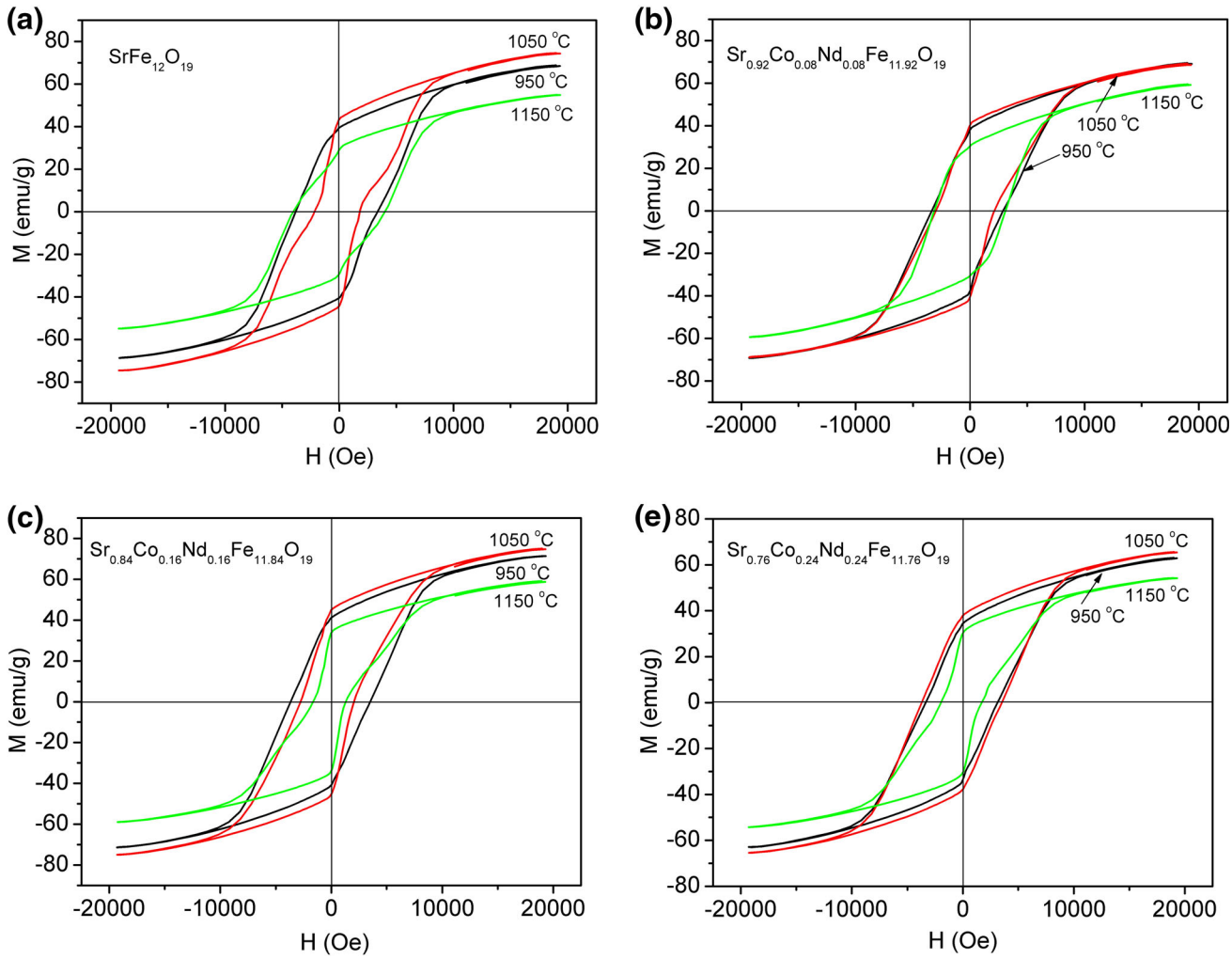

Fig. 6. *M–H* (magnetization–hysteresis) loops of $Sr_{1-x}Co_xNd_xFe_{12-x}O_{19}$ samples obtained at different temperatures in air for 2.5 h: (a) $SrFe_{12}O_{19}$, (b) $Sr_{0.92}Co_{0.08}Nd_{0.08}Fe_{11.92}O_{19}$, (c) $Sr_{0.84}Co_{0.16}Nd_{0.16}Fe_{11.84}O_{19}$, and (d) $Sr_{0.76}Co_{0.24}Nd_{0.24}Fe_{11.76}O_{19}$.

By contrast, coercivity of other compositions $Sr_{1-x}Co_xNd_xFe_{12-x}O_{19}$ (x = 0, 0.08, and 0.24) exhibits non-linear variation with the increase in calcination temperature (Fig. 8b). The trend of coercivity of $Sr_{1-x}Co_xNd_xFe_{12-x}O_{19}$, calcined at 1050°C, increases with the increase in substitution content (x). $SrFe_{12}O_{19}$, calcined at 1150°C, has the highest coercivity value (4037.01 ± 42.39 Oe); $Sr_{0.84}Co_{0.16}Nd_{0.16}Fe_{11.84}O_{19}$, calcined at 1150°C, has the lowest coercivity value (1637.39 ± 17.19 Oe).

The dependence of squareness ($R = Mr/Ms$) on calcination temperature and substitution content (x) is shown in Fig. 9a. Squareness of $Sr_{1-x}Co_xNd_xFe_{12-x}O_{19}$ first increases with the increase in calcination temperature, and then decreases at 1150°C. In addition, the squareness of $Sr_{1-x}Co_xNd_xFe_{12-x}O_{19}$ exhibits non-linear variation with the increase in substitution content (x). The R value of $Sr_{1-x}Co_xNd_xFe_{12-x}O_{19}$ is between 0.5165 ± 0.0041 and 0.6040 ± 0.0048. Correlation between magnetic domain type of ferrites and R value is as follows. Larger R values ($R \geq 0.5$) indicate that ferrite is in a single magnetic domain, and smaller R values ($R < 0.5$) are expected only in the case of the formation of a multi-domain structure.[28,38] Earlier studies have indicated that the single-domain critical size (D_c) for a $SrFe_{12}O_{19}$ particle is about 650 nm,[39,40] which is much smaller than the particle sizes of $Sr_{1-x}Co_xNd_xFe_{12-x}O_{19}$ samples calcined at 1150°C. The R value (R = 0.5165 ± 0.0041) of $Sr_{0.92}Co_{0.08}Nd_{0.08}Fe_{11.92}O_{19}$, calcined at 1150°C, is very close to the critical R = 0.5 value. Therefore, $Sr_{0.92}Co_{0.08}Nd_{0.08}Fe_{11.92}O_{19}$ particles, calcined at 1150°C, also have the possibility of a multi-domain structure; other $Sr_{1-x}Co_xNd_xFe_{12-x}O_{19}$ particles, calcined between 950°C and 1150°C, are of a single magnetic domain. $Sr_{0.84}Co_{0.16}Nd_{0.16}Fe_{11.84}O_{19}$, calcined at 1050°C, has the highest R value (0.6040 ± 0.0048), which is useful for high-density magnetic recording and enhanced memory storage.[37]

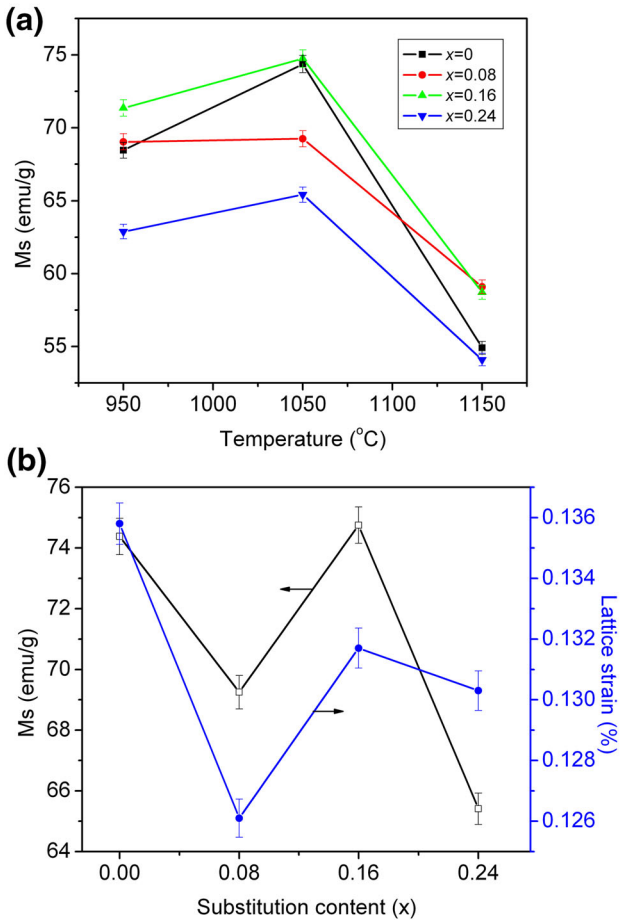

Fig. 7. Dependence of specific saturation magnetization (a) and lattice strains (b) of $Sr_{1-x}Co_xNd_xFe_{12-x}O_{19}$ on substitution content (x).

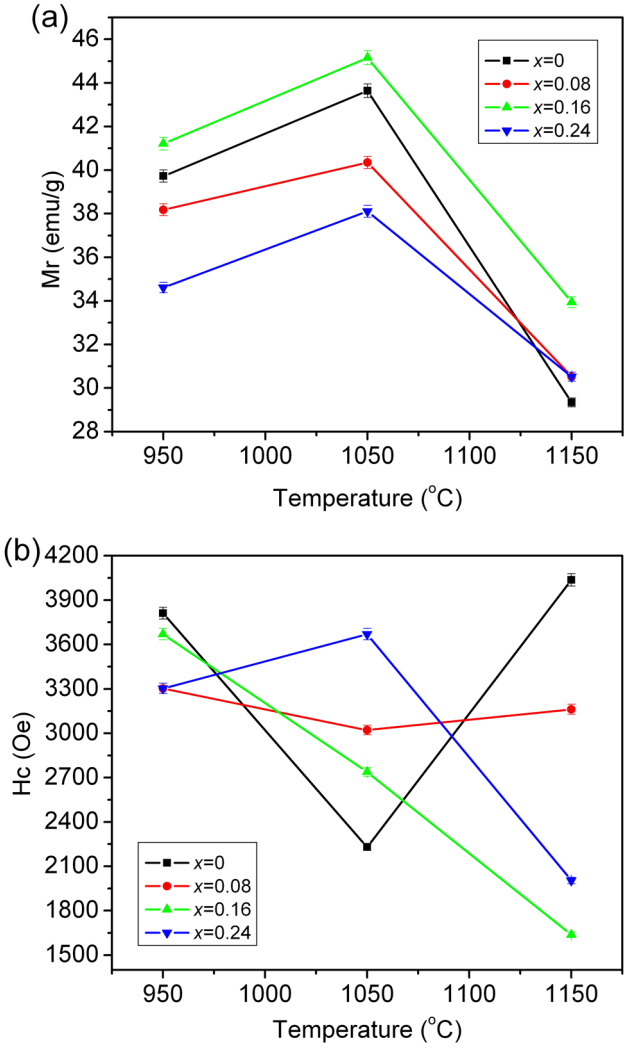

Fig. 8. Dependence of remanence (Mr) (a) and coercivity (Hc) (b) of $Sr_{1-x}Co_xNd_xFe_{12-x}O_{19}$ on substitution content (x) and calcination temperature.

The magnetic moment of $Sr_{1-x}Co_xNd_xFe_{12-x}O_{19}$ samples is estimated using the following relationship[28]:

$$\eta_B = M \times Ms/5585, \quad (6)$$

where M is the molecular weight of the composition, and Ms the specific saturation magnetization (emu/g), and η_B the magnetic moment (μ_B). The variation of magnetic moment (η_B) as a function of calcination temperature and substitution content (x) for $Sr_{1-x}Co_xNd_xFe_{12-x}O_{19}$ is shown in Fig. 9b. The magnetic moment of $Sr_{1-x}Co_xNd_xFe_{12-x}O_{19}$ (x = 0, 0.16, and 0.24) first increases with the increase in calcination temperature, and then decreases at 1150°C. By contrast, the magnetic moment of $Sr_{0.92}Co_{0.08}Nd_{0.08}Fe_{11.92}O_{19}$ decreases with the increase in calcination temperature. The magnetic moment of $Sr_{1-x}Co_xNd_xFe_{12-x}O_{19}$ can be increased by a small amount of substitution, but the magnetic moment value exhibits non-linear variation with substitution content (x). $Sr_{0.84}Co_{0.16}Nd_{0.16}Fe_{11.84}O_{19}$, calcined at 1050°C, has the highest magnetic moment value (14.34 ± 0.11 μ_B); $Sr_{0.76}Co_{0.24}Nd_{0.24}Fe_{11.76}O_{19}$, calcined at 1150°C, has the lowest magnetic moment value (10.42 ± 0.08 μ_B).

The effective anisotropy constant (K_{eff}) is calculated using Eq. 7[28]

$$Hc = 0.985K_{eff}/Ms, \quad (7)$$

where Hc is the coercivity and Ms the specific saturation magnetization. The effective anisotropy constants (K_{eff}) of $Sr_{1-x}Co_xNd_xFe_{12-x}O_{19}$, calcined at 1050°C, are 168,411.4(2) erg/g for x = 0; 210,344.9(9) erg/g for x = 0.08; 207,811.8(3) erg/g for x = 0.16; and 243,711.0(2) erg/g for x = 0.24, respectively. The results show that substitutions of Nd^{3+} and Co^{2+} ions for Sr^{2+} and Fe^{3+} ions can remarkably improve the effective anisotropy constant of $Sr_{1-x}Co_xNd_xFe_{12-x}O_{19}$.

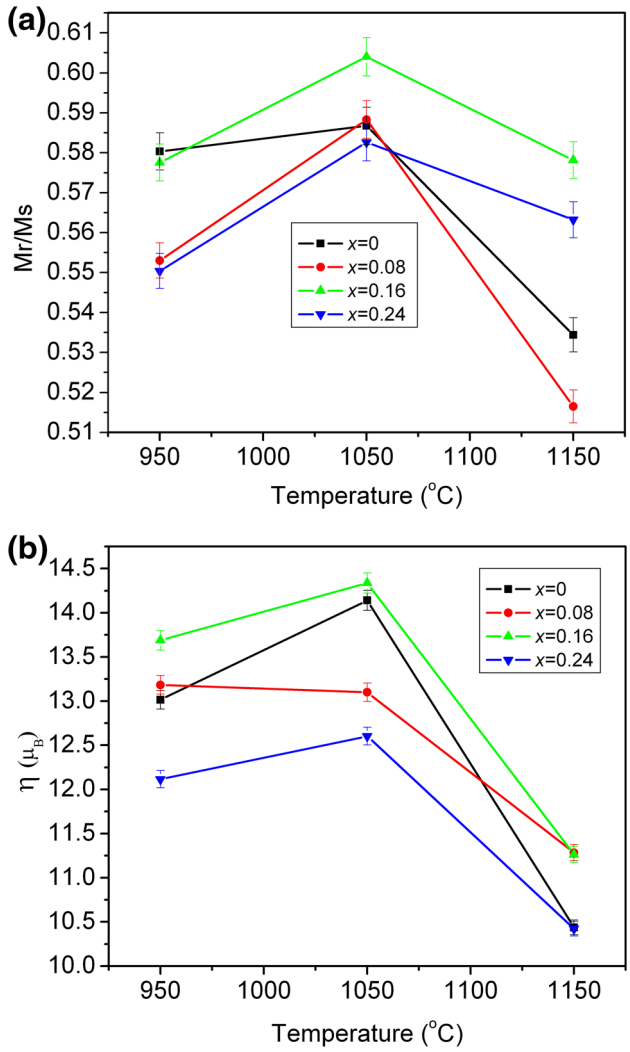

Fig. 9. Dependence of squareness (*Mr*/*Ms*) (a) and magnetic moment (η_B) (b) of $Sr_{1-x}Co_xNd_xFe_{12-x}O_{19}$ on substitution content (x) and calcination temperature.

CONCLUSIONS

Co-Nd substituted M-type Sr hexaferrite with composition $Sr_{1-x}Co_xNd_xFe_{12-x}O_{19}$ (x = 0, 0.08, 0.16, and 0.24) was successfully synthesized by the ball-milling-assisted ceramic process. XRD and SEM analyses confirm the formation of M-type Sr hexaferrite with platelet-like morphology when $Sr_{1-x}Co_xNd_xFe_{12-x}O_{19}$ (x = 0, 0.08, 0.16, and 0.24) precursors are calcined at 950°C in air for 2.5 h. Lattice parameters "a" and "c" values of $Sr_{1-x}Co_xNd_xFe_{12-x}O_{19}$ reflects a very small variation after doping Nd^{3+} and Co^{2+} ions. Average crystallite size of $Sr_{1-x}Co_xNd_xFe_{12-x}O_{19}$ sample, calcined at 1150°C, decreased obviously after substituting Sr^{2+} and Fe^{3+} ions by Nd^{3+} and Co^{2+} ions. This is because the bond energy of Nd^{3+}–O^{2-} is much larger than that of Sr^{2+}–O^{2-}. Magnetic characterization indicates that all the samples exhibit good magnetic properties. Substitution of Sr^{2+} and Fe^{3+} ions by Nd^{3+} and Co^{2+} ions can markedly improve the specific saturation magnetizations, remanence, and effective anisotropy constant of $Sr_{1-x}Co_xNd_xFe_{12-x}O_{19}$. $Sr_{0.84}Co_{0.16}Nd_{0.16}Fe_{11.84}O_{19}$, calcined at 1050°C, has the highest specific saturation magnetization value (74.75 ± 0.60 emu/g), remanence (45.15 ± 0.32 emu/g), and magnetic moment (14.34 ± 0.11 μ_B); $SrFe_{12}O_{19}$, calcined at 1150°C, has the highest coercivity value (4037.01 ± 42.39 Oe). These magnetic parameters make this material a promising candidate for applications such as high-density magnetic recording and microwave-absorbing materials.

ACKNOWLEDGEMENTS

This study was financially supported by the National Natural Science Foundation of China (Grant No. 21603040) and the Guangxi Natural Science Foundation of China (Grant Nos. 2016GXNSFDA380034, 2016GXNSFBA380062).

REFERENCES

1. T.Y. Hwang, J. Lee, H.R. Lim, S.J. Jeong, G.H. An, J. Kim, and Y.H. Choa, *Ceram. Int.* 43, 3879 (2017).
2. F. Rhein, R. Karmazin, M. Krispin, T. Reimann, and O. Gutfleisch, *J. Alloy. Compd.* 690, 979 (2017).
3. M. Cernea, S.G. Sandu, C. Galassi, R. Radu, and V. Kuncser, *J. Alloy. Compd.* 561, 121 (2013).
4. R.C. Pullar, *Prog. Mater Sci.* 57, 1191 (2012).
5. S. Bierlich, F. Gellersenb, A. Jacob, and J. Töpfer, *Mater. Res. Bull.* 86, 19 (2017).
6. G. Qiang, Y. Jin, X.W. Lu, X.P. Cui, D.M. Deng, B.J. Kang, W.G. Yang, S.X. Cao, and J.C. Zhang, *Appl. Phys. A* 122, 681 (2016).
7. R.A. Pawar, S.S. Desai, Q.Y. Tamboli, S.E. Shirsath, and S.M. Patange, *J. Magn. Magn. Mater.* 378, 59 (2015).
8. W. Chen, W.W. Wu, M.M. Mao, C. Zhou, S.F. Zhou, M.Y. Li, and Q. Wang, *J. Supercond. Novel Magn.* 30, 707 (2017).
9. J.R. Liu, R.Y. Hong, W.G. Feng, D. Badami, and Y.Q. Wang, *Powder Technol.* 262, 142 (2014).
10. C.L. Lei, S.L. Tang, and Y.W. Du, *Ceram. Int.* 42, 15511 (2016).
11. J.F. Wang, C.B. Ponton, and I.R. Harris, *J. Alloy. Compd.* 403, 104 (2005).
12. J.F. Wang, C.B. Ponton, and I.R. Harris, *IEEE Trans. Magn.* 38, 2928 (2002).
13. J.F. Wang, C.B. Ponton, and I.R. Harris, *J. Magn. Magn. Mater.* 298, 122 (2006).
14. N. Rezlescu, C. Doroftei, E. Rezlescu, and P.D. Popa, *J. Alloy. Compd.* 451, 492 (2008).
15. S.E.M. Ghahfarokhi, F. Ranjbar, and M.Z. Shoushtari, *J. Magn. Magn. Mater.* 349, 80 (2014).
16. W.M.S. Silva, N.S. Ferreira, J.M. Soares, R.B. da Silva, and M.A. Macêdo, *J. Magn. Magn. Mater.* 395, 263 (2015).
17. A. Thakur, R.R. Singh, and P.B. Barman, *Mater. Chem. Phys.* 141, 562 (2013).
18. K. Praveena, K. Sadhana, H.L. Liu, and M. Bououdina, *J. Magn. Magn. Mater.* 426, 604 (2017).
19. I.A. Auwal, H. Erdemi, H. Sözeri, H. Güngüneş, and A. Baykal, *J. Magn. Magn. Mater.* 412, 69 (2016).
20. M.N. Ashiq, M.J. Iqbal, and I.H. Gul, *J. Alloy. Compd.* 487, 341 (2009).
21. Z.Y. Zhang, X.X. Liu, X.J. Wang, Y.P. Wu, and R. Li, *J. Alloy. Compd.* 525, 114 (2012).
22. L. Peng, L.Z. Li, R. Wang, Y. Hu, X.Q. Tu, and X.X. Zhong, *J. Magn. Magn. Mater.* 393, 399 (2015).
23. T.T. Loan, T.T.V. Nga, N.P. Duong, S. Soontaranon, and T.D. Hien, *J. Electron. Mater.* 46, 3396 (2017).

24. L. Qiao, L.S. You, J.W. Zheng, L.Q. Jiang, and J.W. Sheng, *J. Magn. Magn. Mater.* 318, 74 (2007).
25. K.S. Moon and Y.M. Kang, *J. Eur. Ceram. Soc.* 36, 3383 (2016).
26. A.L. Xia, C.H. Zuo, L. Chen, C.G. Jin, and Y.H. Lv, *J. Magn. Magn. Mater.* 332, 186 (2013).
27. K.W. Zhou, W. Chen, X.H. Wu, W.W. Wu, C.W. Lin, and J. Wu, *J. Electron. Mater.* 46, 4618 (2017).
28. X.H. Wu, W. Chen, W.W. Wu, H.J. Li, and C.W. Lin, *J. Electron. Mater.* 46, 199 (2017).
29. Y.L. Chai, Y.S. Chang, G.J. Chen, and Y.J. Hsiao, *Mater. Res. Bull.* 43, 1066 (2008).
30. X.Z. Guo, H. Yang, M. Cao, C. Han, and F.F. Song, *Trans. Nonferrous Met. Soc. China* 16, 593 (2006).
31. Y. Zhou, X.H. Wu, W.W. Wu, X.S. Huang, W. Chen, Y.L. Tian, and D. He, *Mater. Sci. Semicond. Process.* 41, 162 (2016).
32. S.F. Kong, P.P. Zhang, X.F. Wen, P.H. Pi, J. Cheng, Z.R. Yang, and J. Hai, *Particuology* 6, 185 (2008).
33. G.R. Gordani, A. Ghasemi, and A. Saidi, *Ceram. Int.* 40, 4945 (2014).
34. V.C. Chavan, S.E. Shirsath, M.L. Mane, R.H. Kadam, and S.S. More, *J. Magn. Magn. Mater.* 398, 32 (2016).
35. R. Kumar and M. Kar, *J. Magn. Magn. Mater.* 416, 335 (2016).
36. R. Kumar and M. Kar, *Ceram. Int.* 42, 6640 (2016).
37. K. Rana, P. Thakur, A. Thakur, M. Tomar, V. Gupta, J.L. Mattei, and P. Queffelec, *Ceram. Int.* 42, 8413 (2016).
38. X.H. Wu, W. Chen, W.W. Wu, Y. Ning, and S.S. Chen, *J. Mater. Sci. Mater. Electron.* 28, 18815 (2017).
39. P.P. Jing, J.L. Du, J.B. Wang, J.W. Wei, L.N. Pan, J.N. Li, and Q.F. Liu, *Sci. Rep*. https://doi.org/10.1038/srep15089.
40. Z.F. Zi, Y.P. Sun, X.B. Zhu, Z.R. Yang, J.M. Dai, and W.H. Song, *J. Magn. Magn. Mater.* 320, 2746 (2008).